Phase coexistence and transitions between antiferromagnetic and ferromagnetic states in a synthetic antiferromagnet

C. E. A. Barker,[1,2,*] K. Fallon,[3] C. Barton,[2] E. Haltz,[1] T. P. Almeida,[3] S. Villa,[3] C. Kirkbride,[3] F. Maccherozzi,[4] B. Sarpi,[4] S. S. Dhesi,[4] D. McGrouther,[3] S. McVitie,[3] T. A. Moore,[1] O. Kazakova,[2] and C. H. Marrows[1,†]

[1]*School of Physics and Astronomy, University of Leeds, Leeds LS2 9JT, United Kingdom*

[2]*National Physical Laboratory, Hampton Road, Teddington TW11 0LW, United Kingdom*

[3]*School of Physics and Astronomy, University of Glasgow, Glasgow G12 8QQ, United Kingdom*

[4]*Diamond Light Source, Harwell Science and Innovation Campus, Didcot, Oxfordshire OX11 0DE, United Kingdom*

(Received 5 February 2024; revised 19 March 2024; accepted 20 March 2024; published 26 April 2024)

In synthetic antiferromagnets (SAFs), antiferromagnetic (AFM) order and synthesis using conventional sputtering techniques is combined to produce systems that are advantageous for spintronics applications. Here we present the preparation and study of SAF multilayers possessing both perpendicular magnetic anisotropy and the Dzyaloshinskii-Moriya interaction. The multilayers have an antiferromagnetically aligned ground state but can be forced into a full ferromagnetic (FM) alignment by applying an out-of-plane field ∼100 mT. We study the spin textures in these multilayers in their ground state as well as around the transition point between the AFM and FM states at fields ∼ 40 mT by imaging the spin textures using complementary methods: photoemission electron, magnetic force, and Lorentz transmission electron microscopies. The transformation into a FM state by field proceeds by a nucleation and growth process, where skyrmionic nuclei form and then broaden into regions containing a ferromagnetically aligned labyrinth pattern that eventually occupies the whole film. Remarkably, this process occurs without any significant change in the net magnetic moment of the multilayer. The mix of antiferromagnetically and ferromagnetically aligned regions on the micron scale in the middle of this transition is reminiscent of a first-order phase transition that exhibits phase coexistence. These results are important for guiding the design of spintronic devices whose operation is based on spin textures in perpendicularly magnetized SAFs.

DOI: 10.1103/PhysRevB.109.134437

I. INTRODUCTION

In the field of condensed matter physics, topological spin textures in thin magnetic films, such as skyrmions, have been an area of intense research in recent years [1–4]. From an interest in their fundamental physics to applications in spintronics much effort has been dedicated to studying their properties. In ferromagnetic (FM) thin films these textures can be stabilized by an interfacial Dzyaloshinskii-Moriya interaction (DMI), which is caused by broken symmetry across an interface between the magnetic film and a heavy metal layer [5,6]. The spin textures in these materials, including topologically nontrivial skyrmion textures, have characteristic sizes varying from ∼100 nm up to microns depending on the choice of materials.

These chiral skyrmions exhibit the skyrmion Hall effect, where they move at an angle to the driving force [2], which may prove troublesome for many skyrmionic applications. In order to suppress this effect, the use of synthetic antiferromagnets (SAFs) has been proposed [7,8]. In these systems two magnetic layers are coupled through a nonmagnetic spacer layer by a Ruderman-Kittel-Kasuya-Yosida-type indirect exchange interaction [9], meaning that the net topological charge of a pair of skyrmions in the two layers is zero. The sign of the coupling varies periodically with the thickness of the spacer layer, such that the thickness can be chosen to couple the two layers antiparallel to each other [10]. The near cancellation of the stray field in these materials means that the textures observed in them are predicted to be smaller and more stable and to have lower power consumption [7,8,11]. This was shown for the case of domain wall motion in SAF systems [12–14]. However, the cancellation of the stray field and magnetization in turn means the observation of such topological textures is challenging, and so experimental studies are limited to a handful of results [15–19].

Skyrmions were first observed in synthetic antiferromagnets by carefully tuning the layer thicknesses to the point of transition between out-of-plane (OOP) and in-plane (IP) anisotropy and then using a biasing layer to transform the resulting stripe domain pattern into isolated skyrmions [15]. Since then, skyrmions in SAFs have been observed in unbalanced SAFs [16] and in Co/Pd multilayers [17] using a magneto-optic Kerr effect microscope and a nitrogen vacancy center microscope [18] and in SAFs grown with two magnetic materials using x-ray magnetic circular dichroism (XMCD) scanning transmission x-ray microscopy [19].

*christopher.barker@npl.co.uk

†c.h.marrows@leeds.ac.uk

While the ground state of a SAF has antiferromagnetic (AFM) alignment, an externally applied magnetic field strong enough to overcome the indirect exchange coupling can enforce FM alignment. Very little work has been done on the mechanism of this transition from an AFM to FM state. It is important to properly understand this, considering results are often presented studying SAFs at fields near their transition points. Previous work [20,21] was done on SAFs with perpendicular magnetic anisotropy, showing the transition between the two states; however, this work was performed before the idea of interfacial DMI was commonly known, so that effect was not considered. Moreover, magnetic force microscopy (MFM) alone was used, from which it is difficult to draw quantitative conclusions.

In this work we image a SAF multilayer through its magnetic transitions and show that the mechanism for switching between the AFM and FM states is a defect-driven nucleation process, where FM skyrmions nucleate in the uniform SAF region and expand to include a stripe/skyrmion texture that is ferromagnetically coupled. By using a combination of microscopy techniques sensitive to stray fields above the surface (MFM), the surface magnetic order itself [XMCD photoemission electron microscopy (PEEM)], and the stray field in the entire thickness of the multilayer [Lorentz transmission microscopy (LTEM)], we build a complete picture of the different domain types in these SAFs with DMI. They include a type of skyrmion that exists only in one set of layers in the SAF. In the midst of this external-field-driven transition, the multilayer is subdivided into antiferromagnetically and ferromagnetically aligned regions on the micron scale, reminiscent of phase coexistence during a first-order phase transition. Remarkably, this transition from AFM alignment to a labyrinth domain FM state occurs without any significant change in the net moment as measured by a conventional magnetometer. This work demonstrates the importance of a robust understanding of the transitions between AFM and FM states when applying fields to SAFs. The complete picture of the AFM-FM transitions also represents a different path to understanding the nucleation and control of skyrmions in such SAF systems and even more complex three-dimensional magnetic textures [22,23].

II. METHODS

The multilayer samples were grown in a magnetron sputtering chamber at room temperature with a base pressure of $\sim 10^{-8}$ mbar. The partial pressure of Ar during growth was 3.3×10^{-3} mbar. Typical growth rates of materials were 0.5–1 Å/s, calculated from x-ray reflectivity fits to multilayer calibration samples, with typical powers of 10–20 W. The samples were deposited on thermally oxidized Si with a nominal oxide thickness of 100 nm. Initially, a seed layer of Ta was deposited, followed by a repeating stack structure of [Ru(5)/Pt(10)/CoFeB(10)/Ru(5)/Pt(10)/CoB(13)]×10, with layer thicknesses given in angstroms, and then capped with a layer of Ru followed by Pt, as depicted in Fig. 1(a). Figures 1(b) and 1(c) show the high quality of the deposited multilayer, especially given the ultrathin subnanometer layers and large number of repetitions. The thickness of the Ru spacer was chosen to result in the maximum possible

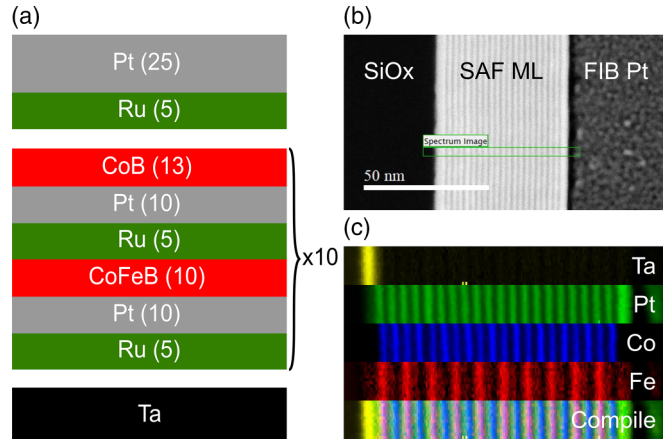

FIG. 1. SAF multilayer structure. (a) SAF multilayer stack, with numbers in brackets denoting layer thicknesses in angstroms. (b). TEM image of a cross section showing a SAF multilayer deposited on top of an Si/SiO_x substrate. (c). EELS chemical map from the box region in (b) displaying the elemental distribution of tantalum, platinum, cobalt, and iron.

antiferromagnetic coupling strength, while the Pt thickness was tuned to be as thin as possible to reduce screening of the antiferromagnetic coupling while still providing an interface-induced perpendicular magnetic anisotropy and DMI [24–26]. The thicknesses of the CoB and CoFeB layers were tuned to be as close as possible to magnetic compensation so that the multilayer has no net magnetic moment. The sets of CoB and CoFeB layers can be considered two sublattices of the SAF; compositional differences of this kind were exploited in recent work [14,19] by using the chemical selectivity of x rays to image each sublattice of the SAF.

Two samples were imaged during this study, henceforth referred to as S1 and S2. They were grown using the same recipe presented in Fig. 1(a) but during two different growth runs; small inconsistencies mean that the resultant samples are unlikely to be exactly the same. The SAF stack for S1 was grown on solid Si/SiO_x substrates for PEEM and MFM imaging, while S2 was deposited onto Si_3N_4 membrane windows with a thickness of 35 nm and window size of $100 \times 100\ \mu m^2$ for imaging in the transmission microscope (TEM). Identical S2 multilayers were simultaneously grown on solid Si/SiO_x for TEM cross-sectional analysis.

The $M(H)$ loops presented in Fig. 2 were measured in a Quantum Design superconducting quantum interference device (SQUID) vibrating sample magnetometer (VSM), where the sample was mounted in a straw, allowing the measurement of its out-of-plane moment in typical fields of ±500 mT at room temperature. The magnetization was calculated by dividing the measured moment by the sample volume. The thickness of the sample was calculated by summing the magnetic layer thicknesses derived from fits to the x-ray reflectivity curve of the sample (not shown). The sample surface area was extracted from a photograph of the sample. It is estimated that the systematic error from these measurements on the magnetization is 6%.

Images at and close to zero field in Fig. 3 were acquired using XMCD-PEEM on beamline I06 at Diamond Light Source.

The sample was mounted in a cartridge capable of applying field pulses up to 60 mT and imaging in static fields up to 10 mT.

Imaging of the transition between the SAF and FM states in Fig. 4 was performed using an Ntegra Aura scanning probe microscope. A commercial low-moment probe was used, with a magnetic coating of 40 nm CoCr and a tip radius of 25–30 nm. Imaging was performed in a standard two-pass system, in which, first, topographical data was obtained and then the tip was lifted and moved over the same row to collect phase information for the MFM. After this, in order to minimally perturb the magnetic textures during imaging, the probe was retracted, and a second magnetic force microscope image was obtained, calculating the lift height by fitting a plane to the topography of the imaging area. In addition, in order to reduce perturbations to the magnetic texture from repeated tip-sample interactions, a new area of the sample was chosen to take each image in order to preserve the originality of the magnetic state as much as possible.

A cross-sectional TEM lamella was prepared from a sister sample to S2 grown on a Si/SiO_x substrate and transferred onto a Cu TEM grid using a Thermo Fisher Helios Xe-plasma focused ion beam instrument. The TEM analysis in Fig. 1 was carried out on a JEOL Atomic Resolution Microscope (JEM-ARM200cF) scanning transmission electron microscope (STEM) operating at 200 kV. This microscope is equipped with a cold field emission gun and a CEOS (Corrected Electron Optical Systems GmbH) probe corrector for STEM imaging. High-angle annular dark-field imaging and electron energy loss spectroscopy (EELS) analysis provided the localized elemental distribution within the SAF multilayer. The DIGITAL MICROGRAPH software package was used to analyze the EELS spectrum images, and noise filtering was performed using a principle component analysis plug-in.

Fresnel images and four-dimensional STEM differential phase contrast (DPC) images were acquired on the same microscope operated in field-free mode. The Fresnel images were collected on a Gatan Orius CCD camera, while the DPC data were collected on a MerlinEM hybrid-pixelated detector, and induction maps were produced using a cross-correlation method [27]. To image in static fields, the objective lens of the microscope is weakly excited and acts as a field source. For all Lorentz TEM methods (Fresnel and DPC) to produce contrast, the sample has to be tilted with respect to the electron beam (and optic axis), resulting in a small in-plane component to any applied field [28–30]. The Fresnel images in Fig. 5 were acquired with a defocus of 2.2 mm. DPC images shown in Fig. 6 were acquired with a 0.88 mrad semiangle, giving a 3.5 nm probe, sampled with a 6.2 nm pixel size; all images referenced in Table I were acquired with a 1.0 mrad semiangle, giving a 3.5 nm probe, sampled with a 4.6 nm pixel size.

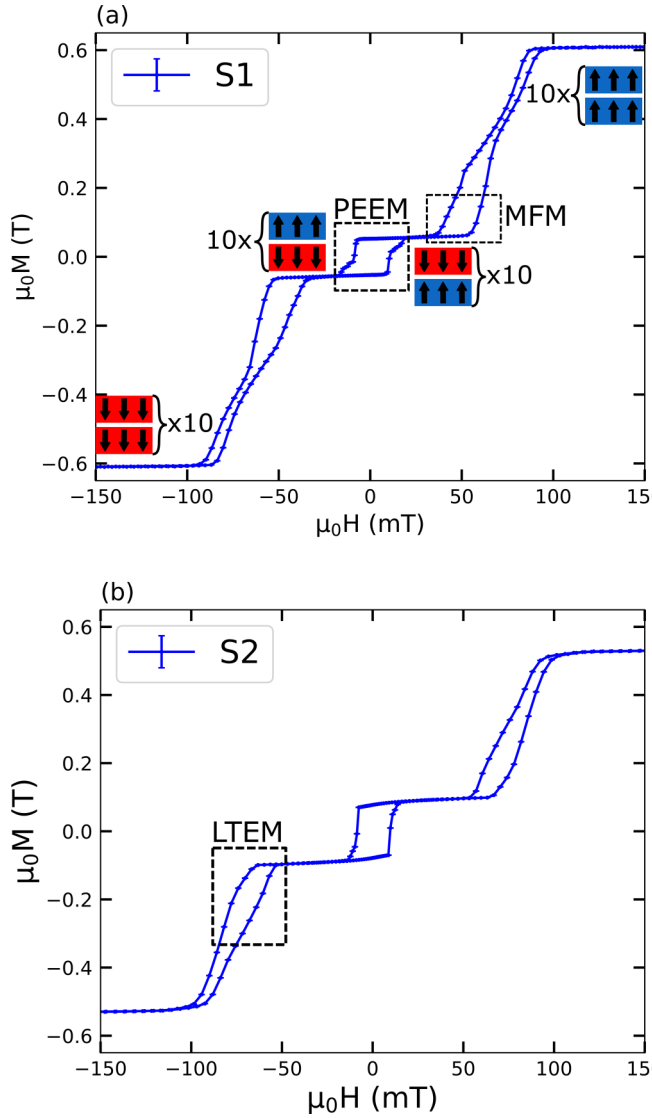

FIG. 2. SQUID VSM $M(H)$ loops at room temperature of the two samples: (a) data for S1 and (b) data for S2. Standard errors from the measurement of magnetization are presented; in addition, there is a systematic error from the volume normalization that is estimated to be 5%. (a) also includes a pictorial description of the magnetic state in each pair of SAF coupled layers at each step of the loop. Dashed boxes show the approximate regions of interest for the three microscopy techniques in Figs. 3–6. Here S1 and S2 are two samples grown in separate runs using the same nominal growth recipe as described in the text.

III. RESULTS AND DISCUSSION

A. Magnetometry

The room temperature $M(H)$ hysteresis loops of the two samples are presented in Fig. 2. The saturation magnetizations of each sample, measured in teslas, are 0.61 ± 0.04 T for S1 and 0.53 ± 0.03 T for S2. The quoted error includes the contribution of a systematic error in the calculation of the sample volume, whereas the error bars in Fig. 2 show the random error of only the SQUID VSM measurement. This difference of 13% in the magnetization corresponds to the small differences between the two growths. The sample retains its compensation in out of plane fields up to ∼50 mT before the net magnetization gradually begins to increase over a wide range of field before saturating at ∼100 mT, beyond which the applied field is strong enough to enforce a fully FM alignment of the layers. There is observable hysteresis in the transition from AFM to FM alignment.

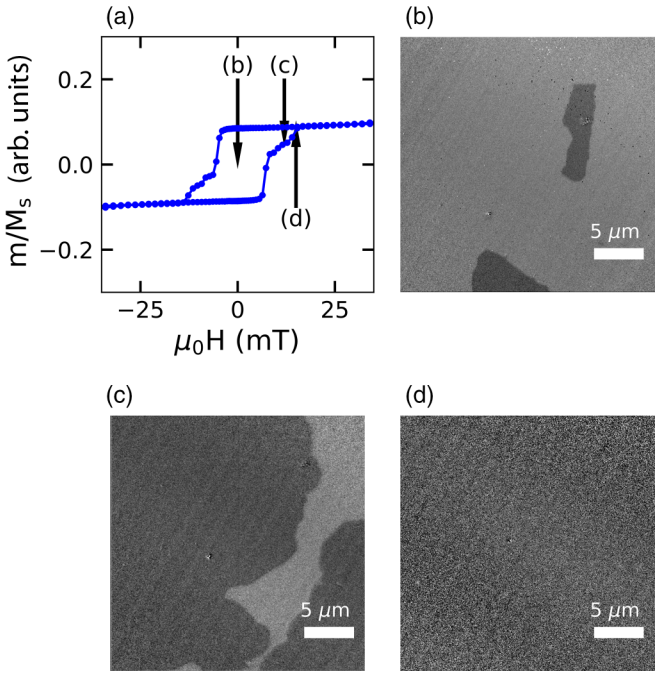

FIG. 3. PEEM imaging of remanent SAF states. (a) Magnified view of the low-field region of the $M(H)$ loop in Fig. 2(a), showing the transition between the two remanent SAF states. Arrows show the fields applied prior to acquiring images at remanence. photoemission electron microscope images taken at zero field after (b) an alternating demagnetization cycle, (c) an applied field of +12 mT, and (d) an applied field of +15 mT.

Below the field at which the antiferromagnetic alignment is stable there is an additional switch in the loop owing to imperfect compensation of the moments of the two sublattices. Thus, as the field is swept through zero, the layers spontaneously reorder themselves into an opposite AFM configuration, such that they retain their AFM alignment, but each sublattice has the opposite orientation. This process is depicted schematically alongside the data in Fig. 2. From these measurements alone, which lack spatial resolution, the nature of the remanent SAF state is unclear, as well as the nature of the transformation from the AFM to FM state.

B. PEEM imaging of the SAF state

The magnetic state of the sample was imaged at remanence using PEEM. The surface sensitivity of this technique means that only the very topmost magnetic layer is imaged. This was confirmed by collecting x-ray absorption spectra from the secondary electrons for photon energies across both the Co and Fe L edges (not shown). This showed clear peaks for Co but no signal for Fe, showing that only the CoB layer immediately under the cap yields a signal, not the CoFeB layer below it. All the images presented in Fig. 3 were taken at the Co L_3 edge. Due to the difficulties of PEEM imaging in a magnetic field we returned to zero field after applying a field history in order to acquire each image.

In order to observe any magnetic contrast in the SAF state, the sample was first prepared using an alternating demagnetization cycle, applying sequential field pulses of opposite polarity and diminishing amplitude, starting at the maximum field of the cartridge (60 mT), outside the SAF region of the sample, and finishing at zero field. Imaging the sample after this protocol yields large domains pinned around structural defects in the sample as shown in Fig. 3(b). We interpret the image in Fig. 3(b) as showing domains of the two alternative SAF configurations depicted schematically in Fig. 3.

In Fig. 3(c) we show the same image area after an applied field of 12 mT, where the dark domains from Fig. 3(b) have expanded to cover almost the entirety of the image area. These dark domains must therefore be the ones in which the small net moment of the SAF is aligned with the direction of the applied field. After an applied field of 15 mT [Fig. 3(d)] we see that these domains have expanded to cover the entire image area, and it is uniformly saturated into one of the two uniform AFM configurations. Similar images lacking any magnetic contrast were always obtained whenever the remanent state on the major hysteresis loop was imaged.

These large defect-pinned domains at zero field in the SAF state are in contrast to conventional ferromagnetic multilayers. In these systems a complex domain pattern forms at zero field [5,31] which can typically be reduced to isolated skyrmions as the field is increased to near saturation. This complex pattern is a result of the competition between the various magnetic energy terms: exchange, DMI, anisotropy, and the effect of the demagnetization field.

C. MFM imaging of the transition between the SAF and the ferromagnetic state

The images acquired using PEEM in Fig. 3 are complemented by magnetic force microscope images taken under an applied out-of-plane field. These images are presented in Fig. 4. Figure 4(a) shows the region of interest of the $M(H)$ loop, which is around where the measured moment starts to rise on the increasing field sequence of the hysteresis loop. Images are reported at the field applied to the sample during measurement; however, the true field is likely to be of the order of 5–10 mT larger than this due to the effect of the field from the tip [32,33]. Magnetic force microscope images at this range of field are shown in Figs. 4(b)–4(f).

Figure 4(b) shows the sample in a uniform SAF state with no observable magnetic texture. This is consistent with the photoemission electron microscope images, from which we know that the SAF state is laterally very uniform at this point in the loop. The total magnetization of the structure is nonzero due to small differences between the moments of the individual materials, as discussed. As the field increases, magnetic bubbles begin to nucleate, as shown in 4(c). We suggest that structural defects present in the topographical scans (not shown) drive this bubble formation. They have the appearance of skyrmionic domains with their core pointing in the direction of the applied field.

As the field continues to rise, these bubbles are stripped out by linear expansion into worm domains [Fig. 4(d)], which then begin to widen. On passing a critical width of ∼0.5 μm they begin to subdivide into more complex textures that contain labyrinth patterns and some small circular features that we

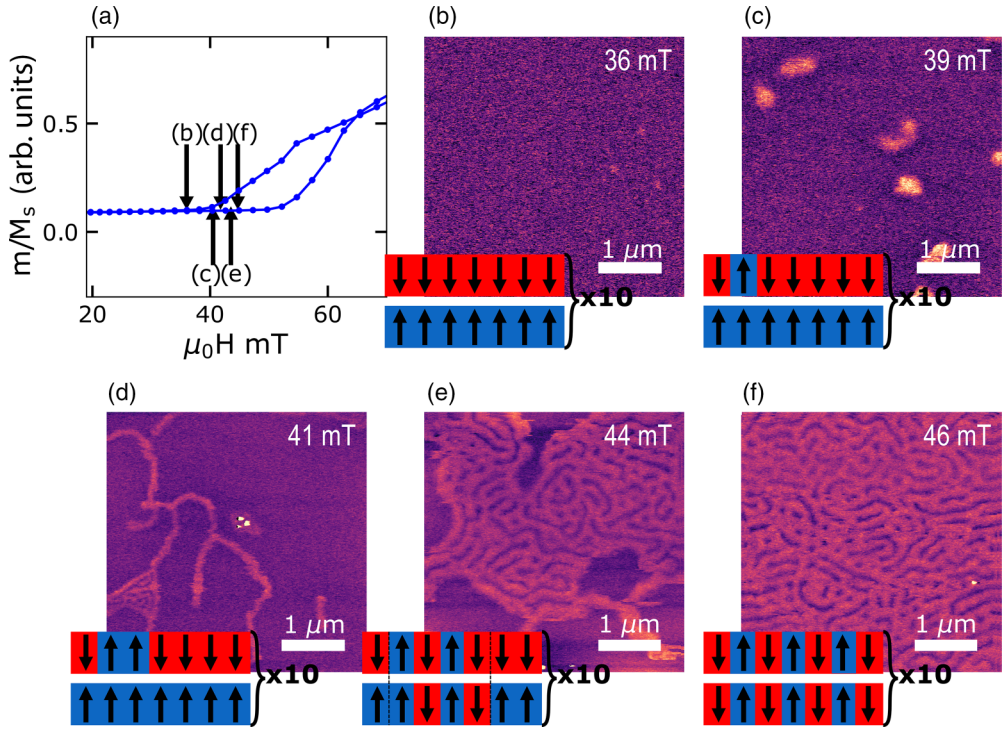

FIG. 4. MFM imaging of AFM-FM phase coexistence. (a) Magnified view of the transition region of the $M(H)$ loop in Fig. 2(a), showing the transition from the SAF state of the sample into the FM state, and the fields applied during MFM imaging. Magnetic force microscope images acquired at applied out-of-plane fields of (b) 36, (c) 39, (d) 41, (e) 44, and (f) 46 mT. There is likely a small offset in the true field experienced by the sample area due to the stray field of the tip that is expected to be ∼10 mT. The associated schematics show the nature of the coupling at each image. Initially, a section of one layer flips into FM alignment, then grows and starts to encompass domain structure, which goes on to expand over the whole image area.

interpret as being skyrmions. The beginning of this process can be seen in the small triangular region in the bottom left of Fig. 4(d). In Fig. 4(e) most of the film has filled with these textures, but some uniform-contrast antiferromagnetically aligned regions still remain. In Fig. 4(f) the entire film is filled with these labyrinthine patterns, reminiscent of a conventional, non-SAF multilayer. Since demagnetizing effects must be driving this domain formation, we take these data as indicating that the magnetization now has a FM alignment between layers throughout the film.

The fact that the net magnetization does not noticeably increase over the field range in which these images were taken means that these textures cannot possess any significant net moment. Indeed, while we interpret the image at 36 mT [Fig. 4(b)] as showing a SAF state that is laterally uniform but in which the magnetization alternates vertically from layer to layer, we interpret the image at 46 mT [Fig. 4(f)] as showing a FM state that is vertically uniform but in which the magnetization alternates laterally from domain to domain. Schematics are shown together with each panel to support this explanation.

Figures 4(c)–4(e) therefore show intermediate states between the fully antiferromagnetically aligned phase in Fig. 4(b) and fully ferromagnetically aligned phase in Fig. 4(f), in which there is phase coexistence of antiferromagnetically and ferromagnetically aligned regions. We can interpret the patches of bright contrast in Fig. 4(c) as being nuclei of the FM phase within the uniform AFM background. Interestingly, they must consist of skyrmions in the sublattice that have reversed into the field direction, while the other sublattice remains uniform. These nuclei elongate [Fig. 4(d)] through the strip-out mechanism. As the sample moves out of the SAF state and the antiferromagnetic coupling is overcome, the individual layers are no longer screened from the rest of the stack, and so the effect of the demagnetization field can no longer be neglected. This causes the formation of a domain structure within the ferromagnetically aligned regions [Figs. 4(d)–4(f)], where the sample is still magnetically compensated, albeit laterally through the domains instead of vertically between uniform layers. After this the sample then goes on to behave like its ferromagnetic equivalent, exhibiting the well-characterized transition from a mix of wormlike domains to isolated skyrmions to being fully saturated.

This is of interest since the onset of the transformation from AFM to FM alignment is not accompanied by a clear signature in the measurement of bulk magnetization. We support this picture with the schematics presented along with each magnetic force microscope image. The initial bubbles will generate a small net moment; however, it is negligible, as they represent a tiny fraction of the whole sample, as seen in the schematic in Fig. 4(c). When these ferromagnetic regions cover a non-negligible area of the film [schematic in Fig. 4(e)], the stripe texture formed within them is laterally fully compensated (albeit vertically ferromagnetically aligned) so that they contribute no net magnetization. This continues until the stripe texture encompasses the whole film

[schematic in Fig. 4(f)], where the entire area is vertically aligned but laterally fully compensated and thus continues to exhibit no net magnetization. It is only around fields of 50–60 mT that the magnetization begins to increase, which is caused by the shrinking of these ferromagnetic stripes into isolated skyrmions, which are in turn annihilated, leaving only a field-polarized state. This discontinuous transition from SAF to ferromagnet is analogous to a first-order phase transition, where the system exhibits phase coexistence and hysteresis.

D. Lorentz imaging of the transition between the SAF and ferromagnetic states

1. Fresnel mode imaging

To substantiate this interpretation of the magnetic force microscope images of sample S1, we performed Fresnel mode Lorentz microscopy on a similar sample, sample S2, grown on an electron-transparent membrane. The two hysteresis loops shown in Fig. 2 show nearly identical features at similar values of applied field, so we can be confident that there are only minor quantitative differences between the samples.

Fresnel mode imaging of the equivalent AFM to FM transition in S2 is shown in Fig. 5, where imaging is nonperturbative and therefore the evolution of the magnetic texture can be observed directly. To produce contrast the sample is tilted 24.1° from the optical axis. The direction and axis of the tilt are shown in Fig. 5(a). In this imaging mode contrast arises from the convergence (bright contrast) or divergence (dark contrast) of electrons transmitted through the sample, and therefore, regions with contrast signify areas where the thickness integrated magnetic induction is changing, i.e., domain walls or boundaries between AFM and FM alignment. This means an isolated FM domain, which would appear as a single strip of contrast in MFM, appears as parallel stripes of dark and bright contrast. A FM worm domain in the center of Fig. 5(a) has been nucleated at this field. This is analogous to the bubbles observed with MFM, where here the tilting of the sample in the field has elongated it into a wormlike domain. On either side of it we see worms that have broadened and filled with a stripe domain pattern. All of these regions expand in Figs. 5(b) and 5(c), beginning to contain the more complex stripe domain textures also seen with MFM.

We should note that while PEEM is sensitive to the sample surface and MFM senses stray fields above that surface, Lorentz contrast arises from electrons that are transmitted through the sample and thus experience deflection contributions from the magnetic induction summed through every layer. In order to confirm that this transition happens in all layers simultaneously, we turn to DPC imaging of the different magnetic states presented so far to provide quantification of the magnetic induction configurations associated with these states.

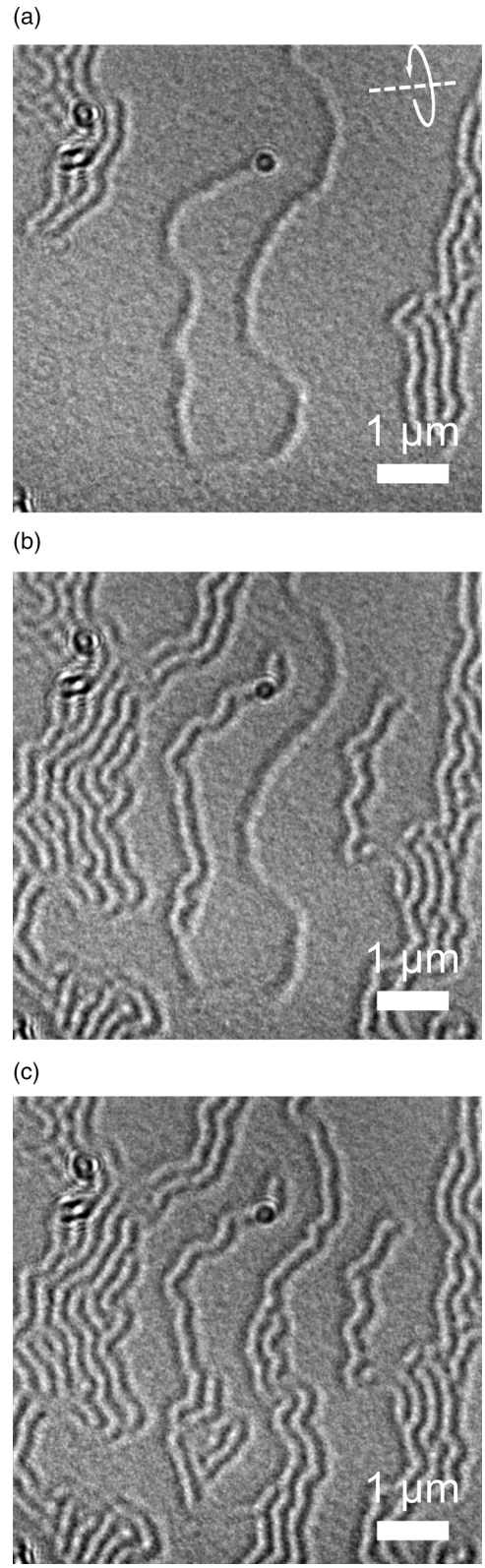

FIG. 5. Fresnel LTEM images of S2 around the transition from AFM to FM alignment, showing the same sample area in each image with the domains growing to encapsulate more complex textures. The bubblelike features are structural defects in the imaging area. Fields the images were measured in were (a) −67.2, (b) −69.1, and (c) −69.7 mT, applied out of plane with respect to the sample. The dashed line and arrow in (a) represent the axis and direction of tilt of imaging.

2. DPC: Quantitative analysis of the mixed-phase state

DPC imaging permits quantitative mapping of the magnetic induction of the sample in transmission and is therefore complementary to MFM imaging, which probes the stray field above the sample. A DPC image of S2 is shown in Fig. 6(a), which corresponds to a similar part of the transition in S1

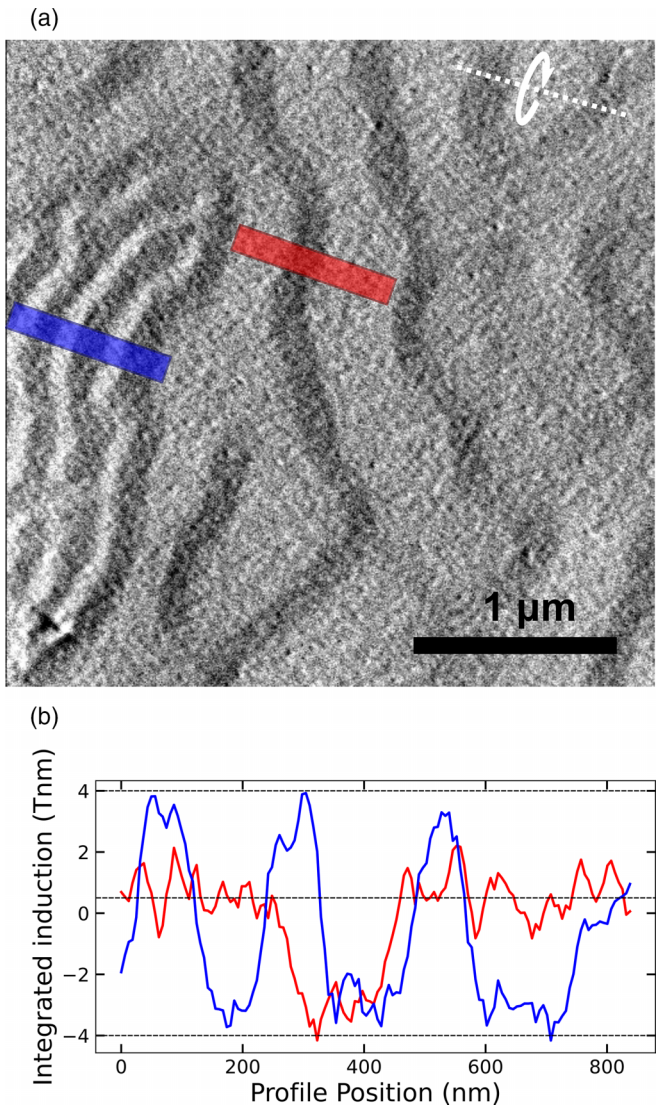

FIG. 6. Quantitative imaging of the mixed-phase state using DPC Lorentz TEM. (a) DPC image of S2 at an applied field of −69.1 mT. The dashed line in the top right corner shows the tilt axis, and the arrow shows the direction of the IP field. (b). Line traces of the integrated inductance through the two regions shaded in (a). Horizontal dashed lines are guides to the eye at ±4 and 0.5 T nm.

imaged with MFM in Figs. 4(d) and 4(e), offset in field due to small differences between S1 and S2. In this imaging mode an isolated domain will appear as a single strip of dark or bright contrast, like that near the center of the image spanned by the red bar, while a multidomain pattern will appear as alternating strips of dark and bright contrast, like those spanned by the blue bar.

Before imaging, the sample was saturated in a strong positive field; then the image in Fig. 6(a) was taken with a sample tilt of 18.9° in an out-of-plane field of −69.1 mT. Note that because of the sample tilt, there is a small in-plane component to the field which biases the direction of domain formation. Three predominant contrast levels are present in the DPC image: almost white contrast, associated with an integrated induction of just under +4 T nm; almost black contrast, associated with an integrated induction of just above −4 T nm; and a medium-gray contrast which averages at about +0.5 T nm. The black and white areas on the left have the typical character of a ferromagnetic multidomain stripe state. As seen from the line traces in Fig. 6(b), the black bands on the right of the image (red line trace) are associated with the same negative integrated induction as the multidomain stripe state (blue line trace), while the gray areas are associated with a small positive integrated induction. This small positive induction is consistent with the residual moment of the slightly unbalanced SAF. Thus, we deduce that the gray areas correspond to a retained antiferromagnetic alignment of the layers and cement the idea that the transition occurs via the defect-driven formation of single-domain FM bubbles that strip out into worms (the black filaments) and subsequently broaden into FM regions subdivided into stripe domains (the alternating black and white stripes).

TABLE I. Integrated inductance of the stripe domains as a function of the applied field.

OOP field (mT)	Integrated induction (T nm)
−69.1	9.6 ± 0.6
−77.5	10 ± 1
−85.2	11 ± 1
−91.2	10 ± 1
−106.6	10 ± 1

A series of DPC images was taken at various points in the transition, and the integrated induction of the multidomain areas was measured as a function of applied field. A comparison of the maximum integrated induction over the transition reveals whether the transition occurs layer by layer or as an abrupt and complete switch. This was done by fitting a number of profiles similar to the blue one in Fig. 6(b) to determine the maximum Lorentz deflection from the domains. The average domain deflection was recorded and divided by $\tan(\theta_{\text{tilt}})$ to compensate for the tilt angle, which gives the integrated induction within the domains. The results are summarized in Table I, which shows, for each DPC image where a multidomain stripe state was observed, the same maximum and minimum thickness integrated magnetic induction. This confirms that the abrupt switch from AFM alignment to FM alignment happens in every layer of the system at once. Since it has been determined that all layers contribute to the integrated induction in the stripe domain areas, the saturation induction can be calculated. From the structure in Fig. 1 we can see that there is a total of 23 nm of magnetic material in the stack. Therefore, the full saturation induction in the magnetic layers inferred from the DPC imaging takes an average value of 0.44 ± 0.04 T, consistent within 2σ with the measured value of the multilayer of 0.53 ± 0.03 T.

IV. CONCLUSION

We used a range of complementary microscopy techniques to gain further insights into the magnetic behavior of perpendicularly magnetized SAFs, focusing on the part of the $M(H)$ loop where AFM order is transformed to FM order by

an applied field. In the AFM configuration the anisotropy of the individual layers dominates, which, together with the lack of magnetostatic field, prevents the formation of skyrmions. This leaves defect-pinned domain walls between the two possible antiferromagnetic states in otherwise laterally uniform regions as the only possibility of an antiferromagnetic magnetic texture. Thus, we conclude that in such samples the stabilization of skyrmions or other small chiral spin textures in the SAF phase by global magnetic fields alone is impossible and requires either a careful tuning of the layer thickness to eliminate the effective anisotropy as in [15] or the application of a local stimulus such as a current pulse [19]. This is a characteristic property of these materials and an important consideration for the design of future SAF spintronic devices.

Images at higher fields around the AFM-FM transition point showed that complex ferromagnetic textures in these samples are possible and highly likely to be chiral based on the strong DMI usually observed at interfaces with Pt [34] and the characteristics of the Fresnel mode images of the domains [28]. We showed that the transition into the ferromagnetic phase occurs via a nucleation and growth mechanism, where there is interestingly no change in the bulk magnetization of the sample. After a careful consideration of the magnetization as a function of field and comparison with the images near zero field, we are led to conclude that these textures appear in FM-ordered regions. Initially, we found small FM nuclei that resemble skyrmions; as the field increases, these are stripped out into wormlike domains that eventually broaden and collapse into a labyrinth domain state that eventually fills the entire film. After transitioning out of the SAF state, the competition of the demagnetizing field along with the DMI, anisotropy, and applied field allows these complex textures to be stabilized. We further reinforced this understanding by performing quantitative DPC imaging of the domains, confirming their FM nature.

These results are important for interpreting images of skyrmions in SAFs under applied magnetic fields near the transition point and confirming whether they are, in fact, antiferromagnetically coupled. The transition into the FM state takes place in a laterally nonuniform manner, and we observed AFM-FM phase coexistence and hysteresis reminiscent of a first-order phase transition. There is no observable change in the overall magnetization in the $M(H)$ loop while the transition into the ferromagnetically aligned state occurs. It is only once this phase is fully established that the magnetization begins to change as the field is increased, in a manner similar to that in a conventional FM skyrmion multilayer.

The data associated with this publication is available from Research Data Leeds at [35].

ACKNOWLEDGMENTS

This work was supported by EPSRC Grants No. EP/T006803/1, No. EP/T006811/1, No. EP/L015323/1, No. EP/S023321/1, and No. EP/T517896/1. The project also received financial support from the UK Government Department for Science, Innovation and Technology through National Measurement Service funding (Low Loss Electronics). C.E.A.B. also acknowledges funding from the National Physical Laboratory. We thank Diamond Light Source for the provision of beam time under Proposal No. MM-28586-1. We thank W. A. Smith for the preparation of TEM cross sections and J. Barker and G. Burnell for useful discussions about the work.

[1] N. Nagaosa and Y. Tokura, Topological properties and dynamics of magnetic skyrmions, Nat. Nanotechnol. **8**, 899 (2013).

[2] K. Everschor-Sitte, J. Masell, R. M. Reeve, and M. Kläui, Perspective: Magnetic skyrmions - Overview of recent progress in an active research field, J. Appl. Phys. **124**, 240901 (2018).

[3] C. Back, V. Cros, H. Ebert, K. Everschor-Sitte, A. Fert, M. Garst, T. Ma, S. Mankovsky, T. L. Monchesky, M. Mostovoy, N. Nagaosa, S. S. Parkin, C. Pfleiderer, N. Reyren, A. Rosch, Y. Taguchi, Y. Tokura, K. Von Bergmann, and J. Zang, The 2020 skyrmionics roadmap, J. Phys. D **53**, 363001 (2020).

[4] C. H. Marrows and K. Zeissler, Perspective on skyrmion spintronics, Appl. Phys. Lett. **119**, 250502 (2021).

[5] S. Woo, K. Litzius, B. Krüger, M. Y. Im, L. Caretta, K. Richter, M. Mann, A. Krone, R. M. Reeve, M. Weigand, P. Agrawal, I. Lemesh, M. A. Mawass, P. Fischer, M. Kläui, and G. S. Beach, Observation of room-temperature magnetic skyrmions and their current-driven dynamics in ultrathin metallic ferromagnets, Nat. Mater. **15**, 501 (2016).

[6] W. Jiang, G. Chen, K. Liu, J. Zang, S. G. te Velthuis, and A. Hoffmann, Skyrmions in magnetic multilayers, Phys. Rep. **704**, 1 (2017).

[7] X. Zhang, Y. Zhou, and M. Ezawa, Magnetic bilayer-skyrmions without skyrmion Hall effect, Nat. Commun. **7**, 10293 (2016).

[8] X. Zhang, M. Ezawa, and Y. Zhou, Thermally stable magnetic skyrmions in multilayer synthetic antiferromagnetic racetracks, Phys. Rev. B **94**, 064406 (2016).

[9] R. A. Duine, K. J. Lee, S. S. P. Parkin, and M. D. Stiles, Synthetic antiferromagnetic spintronics, Nat. Phys. **14**, 217 (2018).

[10] S. S. Parkin, M. Hayashi, and L. Thomas, Magnetic domain-wall racetrack memory, Science **320**, 190 (2008).

[11] F. Büttner, I. Lemesh, and G. S. D. Beach, Theory of isolated magnetic skyrmions: From fundamentals to room temperature applications, Sci. Rep. **8**, 4464 (2018).

[12] S.-H. Yang, K.-S. Ryu, and S. Parkin, Domain-wall velocities of up to 750 m/s driven by exchange-coupling torque in synthetic antiferromagnets, Nat. Nanotechnol. **10**, 221 (2015).

[13] A. Cohen, A. Jonville, Z. Liu, C. Garg, P. C. Filippou, and S.-H. Yang, Current driven chiral domain wall motions in synthetic antiferromagnets with Co/Rh/Co, J. Appl. Phys. **128**, 053902 (2020).

[14] C. E. A. Barker, S. Finizio, E. Haltz, S. Mayr, P. M. Shepley, T. A. Moore, G. Burnell, J. Raabe, and C. H. Marrows, Domain wall motion at low current density in a synthetic antiferromagnet nanowire, J. Phys. D **56**, 425002 (2023).

[15] W. Legrand, D. Maccariello, F. Ajejas, S. Collin, A. Vecchiola, K. Bouzehouane, N. Reyren, V. Cros, and A. Fert, Room-

temperature stabilization of antiferromagnetic skyrmions in synthetic antiferromagnets, Nat. Mater. **19**, 34 (2020).

[16] T. Dohi, S. DuttaGupta, S. Fukami, and H. Ohno, Formation and current-induced motion of synthetic antiferromagnetic skyrmion bubbles, Nat. Commun. **10**, 5153 (2019).

[17] R. Chen, Y. Gao, X. Zhang, R. Zhang, S. Yin, X. Chen, X. Zhou, Y. Zhou, J. Xia, Y. Zhou, S. Wang, F. Pan, Y. Zhang, and C. Song, Realization of isolated and high-density skyrmions at room temperature in uncompensated synthetic antiferromagnets, Nano Lett. **20**, 3299 (2020).

[18] A. Finco, A. Haykal, R. Tanos, F. Fabre, S. Chouaieb, W. Akhtar, I. Robert-Philip, W. Legrand, F. Ajejas, K. Bouzehouane, N. Reyren, T. Devolder, J. P. Adam, J. V. Kim, V. Cros, and V. Jacques, Imaging non-collinear antiferromagnetic textures via single spin relaxometry, Nat. Commun. **12**, 767 (2021).

[19] R. Juge *et al.*, Skyrmions in synthetic antiferromagnets and their nucleation via electrical current and ultra-fast laser illumination, Nat. Commun. **13**, 4807 (2022).

[20] O. Hellwig, A. Berger, and E. E. Fullerton, Magnetic phase separation in artificial *a*-type antiferromagnetic films, Phys. Rev. B **75**, 134416 (2007).

[21] O. Hellwig, A. Berger, J. B. Kortright, and E. E. Fullerton, Domain structure and magnetization reversal of antiferromagnetically coupled perpendicular anisotropy films, J. Magn. Magn. Mater. **319**, 13 (2007).

[22] M. Grelier, F. Godel, A. Vecchiola, S. Collin, K. Bouzehouane, A. Fert, V. Cros, and N. Reyren, Three-dimensional skyrmionic cocoons in magnetic multilayers, Nat. Commun. **13**, 6843 (2022).

[23] M. Grelier, F. Godel, A. Vecchiola, S. Collin, K. Bouzehouane, V. Cros, N. Reyren, R. Battistelli, H. Popescu, C. Léveillé, N. Jaouen, and F. Büttner, X-ray holography of skyrmionic cocoons in aperiodic magnetic multilayers, Phys. Rev. B **107**, L220405 (2023).

[24] R. Lavrijsen, A. Fernández-Pacheco, D. Petit, R. Mansell, J. H. Lee, and R. P. Cowburn, Tuning the interlayer exchange coupling between single perpendicularly magnetized CoFeB layers, Appl. Phys. Lett. **100**, 052411 (2012).

[25] S. Bandiera, R. C. Sousa, S. Auffret, B. Rodmacq, and B. Dieny, Enhancement of perpendicular magnetic anisotropy thanks to Pt insertions in synthetic antiferromagnets, Appl. Phys. Lett. **101**, 072410 (2012).

[26] E. N. Welbourne, T. Vemulkar, D. C. M. C. Petit, and R. P. Cowburn, Weakly coupled synthetic antiferromagnetic nanodisks with perpendicular magnetic anisotropy for lab-on-chip devices, Appl. Phys. Lett. **119**, 102401 (2021).

[27] M. Krajnak, D. McGrouther, D. Maneuski, V. O'Shea, and S. McVitie, Pixelated detectors and improved efficiency for magnetic imaging in stem differential phase contrast, Ultramicroscopy **165**, 42 (2016).

[28] M. Benitez, A. Hrabec, A. Mihai, T. Moore, G. Burnell, D. McGrouther, C. Marrows, and S. McVitie, Magnetic microscopy and topological stability of homochiral Néel domain walls in a Pt/Co/AlO_x trilayer, Nat. Commun. **6**, 8957 (2015).

[29] S. McVitie, S. Hughes, K. Fallon, S. McFadzean, D. McGrouther, M. Krajnak, W. Legrand, D. Maccariello, S. Collin, K. Garcia, N. Reyren, V. Cros, A. Fert, K. Zeissler, and C. H. Marrows, A transmission electron microscope study of Néel skyrmion magnetic textures in multilayer thin film systems with large interfacial chiral interaction, Sci. Rep. **8**, 5703 (2018).

[30] W. Jiang, S. Zhang, X. Wang, C. Phatak, Q. Wang, W. Zhang, M. B. Jungfleisch, J. E. Pearson, Y. Liu, J. Zang, X. Cheng, A. Petford-Long, A. Hoffmann, and S. G. E. te Velthuis, Quantifying chiral exchange interaction for Néel-type skyrmions via lorentz transmission electron microscopy, Phys. Rev. B **99**, 104402 (2019).

[31] C. Moreau-Luchaire, C. Moutafis, N. Reyren, J. Sampaio, C. A. Vaz, N. Van Horne, K. Bouzehouane, K. Garcia, C. Deranlot, P. Warnicke, P. Wohlhüter, J. M. George, M. Weigand, J. Raabe, V. Cros, and A. Fert, Additive interfacial chiral interaction in multilayers for stabilization of small individual skyrmions at room temperature, Nat. Nanotechnol. **11**, 444 (2016).

[32] S. Zhang, J. Zhang, Q. Zhang, C. Barton, V. Neu, Y. Zhao, Z. Hou, Y. Wen, C. Gong, O. Kazakova, W. Wang, Y. Peng, D. A. Garanin, E. M. Chudnovsky, and X. Zhang, Direct writing of room temperature and zero field skyrmion lattices by a scanning local magnetic field, Appl. Phys. Lett. **112**, 132405 (2018).

[33] A. Fernández Scarioni, C. Barton, H. Corte-León, S. Sievers, X. Hu, F. Ajejas, W. Legrand, N. Reyren, V. Cros, O. Kazakova, and H. W. Schumacher, Thermoelectric signature of individual skyrmions, Phys. Rev. Lett. **126**, 077202 (2021).

[34] M. Kuepferling, A. Casiraghi, G. Soares, G. Durin, F. Garcia-Sanchez, L. Chen, C. H. Back, C. H. Marrows, S. Tacchi, and G. Carlotti, Measuring interfacial Dzyaloshinskii-Moriya interaction in ultrathin magnetic films, Rev. Mod. Phys. **95**, 015003 (2023).

[35] https://doi.org/10.5518/1508.